Deflection of electromagnetic waves by pseudogravity in distorted photonic crystals

Kanji Nanjyo,[1] Yuki Kawamoto,[1] Hitoshi Kitagawa,[1] Daniel Headland,[2,*] Masayuki Fujita,[2,†] and Kyoko Kitamura[1,‡,§]
[1]*Department of Electronics, Kyoto Institute of Technology, Matsugasaki, Sakyo-ku, Kyoto 606-8585, Japan*
[2]*Graduate School of Engineering Science, Osaka University, 1-3 Machikaneyama, Toyonaka, Osaka 560-8531, Japan*

(Received 7 December 2022; accepted 31 July 2023; published 28 September 2023)

We demonstrate electromagnetic waves following a gravitational field using a photonic crystal. We introduce spatially distorted photonic crystals (DPCs) capable of deflecting light waves owing to their pseudogravity caused by lattice distortion. We experimentally verify the phenomenon in the terahertz range using a silicon DPC. Pseudogravity caused by lattice distortion reveals alternative approaches to achieve on-chip trajectory control of light propagation in PCs.

DOI: 10.1103/PhysRevA.108.033522

I. INTRODUCTION

The trajectory of electromagnetic (EM) waves may be deflected by gravitational fields in accordance with Einstein's general relativity [1,2]. These fields are the result of a spacetime distortion [3–5] in the vicinity of massive objects. Such spacetime distortion may also be observed in the adiabatic change of Bloch states. Thus, Dong *et al.* reported that pseudogravity (gravitational effects) can be generated by the deformation of crystals in the lower energy (or frequency) region in an electron system [6]. The key consideration in psuedogravity is that the metric tensor must be identified in terms of effective mass and lattice deformation.

Classically, the propagation of EM waves in transparent media is controlled by the refractive index, and hence a given desired beam trajectory may be obtained by engineering a spatially varying refractive index, thereby realizing a gradient index (GRIN) device. In practice, this may be achieved using metamaterials, which employ subwavelength resonators to artificially engineer both electro- and magnetic permeability for an arbitrary refractive index. This has previously enabled precise control of the propagation of EM waves, such as negative refraction [7], invisibility cloaks [8], beam steering, and birefringence [9–11]. In such transformation optics, the metric tensor is generally identified in terms of the spatial distribution of the effective refractive index [7,12–15], and the general relativity, utilizing the metric tensor, has served as a valuable theoretical tool in device design [16].

Photonic crystals (PCs) are a type of artificial material that are constructed by periodically arranging two or more dielectric media with different relative permittivities. PCs have an exotic optical property, i.e., a photonic band structure that corresponds to their periodicity. In contrast to a uniform medium, the group velocity of light waves propagating in a PC is defined by its photonic band structure, and this can be exploited for novel effects. For instance, the dispersion relation in the vicinity of photonic band edges may be tailored to produce phenomena such as negative refraction [17] and the superprism effect [18–21]. The latter is a phenomenon wherein the refractive angle changes rapidly according to variations in the frequency and incident angle due to an anisotropic dispersion relation. However, the dispersion relation is isotropic in the low-frequency region, similar to the relation in a uniform medium.

Recently, we defined a PC that exhibits adiabatic change in the lattice constant as a distorted PC (DPC) and discussed the propagation of light waves from the viewpoint of differential geometry [22]. In this system the metric tensor is identified in terms of effective refractive index caused by lattice distortion. Therefore, the solutions of the geodesic equation reveal that the light trajectory curves in the low-frequency range for a DPC, and a comparable (nondistorted) PC, the light propagation is linear. This bending can be referred to as pseudogravity caused by lattice distortion in a photon system, as it is directly analogous to the effect of gravitational fields under general relativity. In other words, the lattice distortion induces an anisotropic dispersion relation, even in the low-frequency isotropic region of PC. The aim of this paper is to experimentally demonstrate EM wave deflection in DPCs, owing to the pseudogravity.

II. LIGHT PROPAGATION IN DPCS

The square-lattice PC has lattice points represented by $x^{(m)} = ma^{(0)}$ and $y^{(n)} = na^{(0)}$, where $a^{(0)}$ is the lattice constant, and m and n are the numbers of lattice points in the x and y directions, respectively. Here, we discuss a unidirectional DPC for which the lattice point position is distorted by

$$x^{(m)} = ma^{(0)},$$
$$y^{(n)} = \begin{cases} na^{(0)} + n^2\, a^{(0)}\beta & (n \geqslant 0) \\ na^{(0)} & (n < 0) \end{cases}, \tag{1}$$

*Department of Electronic Technology, Universidad Carlos III de Madrid, Leganés, 28911 Madrid, Spain.
†fujita@ee.es.osaka-u.ac.jp
‡kyoko.kitamura.c2@tohoku.ac.jp
§Present address: Graduate School of Engineering, TOHOKU University, 6-6-05 Aramaki Aza Aoba, Aoba-ku, Sendai, Miyagi 980-8579, Japan.

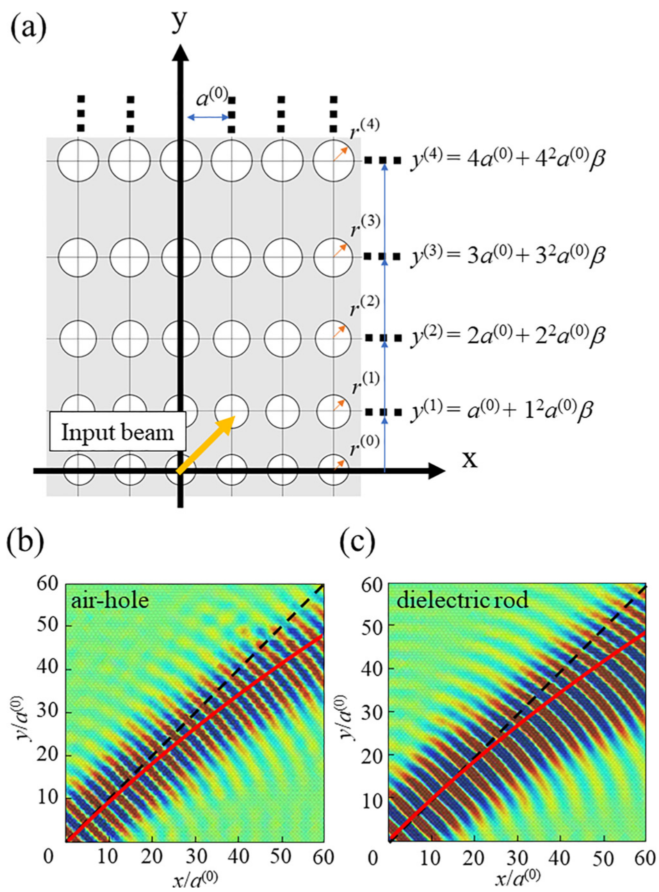

FIG. 1. (a) Schematic of lattice point positions of the DPC based on a square-lattice PC. The DPC introduces a lattice distortion in which the interval of lattice points gradually expands in the $+y$ direction. The x and y axes are defined along the Γ-X direction of the square-lattice PC. To obtain a homogenous and averaged refractive index, the radii increase along the $+y$ direction. (b, c) Simulation results of light propagation in the DPC with $\beta = 0.005$ (H mode): (b) air-hole DPC and (c) dielectric rod DPC. The light wave propagates with the same degree of bending in both results. The solid red lines show the exact solutions of the geodesic equation derived in Ref. [22]. The dashed black lines show the straight lines of input beam direction.

where β is the dimensionless distortion coefficient, which represents the magnitude of lattice distortion. To maintain the Bloch state, β should be sufficiently smaller than 1. In Eq. (1) it is demonstrated that the interval between each lattice position gradually increases in proportion to the number of lattice points in the y direction, as shown in Fig. 1(a). If the lattice point radii are kept constant, this change in interval affects the refractive index along the y direction, similar to a GRIN structure [23,24]. However, to isolate the effect of lattice distortion, we compensate for the change in pitch by modifying the hole radius, while maintaining a constant lattice filling factor (FF), as given by

$$FF = \frac{\pi (r^{(n)})^2}{a^{(0)} a^{(n)}} = \text{const}, \tag{2}$$

where $r^{(0)}$ represents the lattice point radius of the square-lattice PC. The lattice constant along x direction is denoted by $a^{(0)}$, while the lattice constant of the nth lattice point along the y direction is expressed as follows:

$$a^{(n)} = \frac{y^{(n+1)} - y^{(n)}}{2} + \frac{y^{(n)} - y^{(n-1)}}{2} = \frac{y^{(n+1)} - y^{(n-1)}}{2} = a^{(0)}(1 + 2n\beta), \tag{3}$$

where the term $r^{(n)}$ represents the lattice point radius of the nth lattice point and is given by

$$r^{(n)} = r^{(0)}\sqrt{1 + 2n\beta} \quad (n \geqslant 0). \tag{4}$$

Thus, refraction effects due to variation in effective index are avoided.

The simulation results of light propagation in the adaptive air-hole and dielectric rod DPC are shown in Figs. 1(b) and 1(c), respectively. The DPCs were characterized by the following parameters: lattice point radius $r^{(0)}/a^{(0)} = 0.4$, $\beta = 0.005$, and dielectric constant $\varepsilon_1 = 12.25$ (or 1), $\varepsilon_2 = 1$ (or 12.25). A Gaussian beam was used as input at an incident angle of 45° from the x axis (Γ-M direction). To minimize diffraction effects and excessive beam expansion, the input beam width was set to $w_0 = 2\lambda_0$, where λ_0 is the free space wavelength. The figures indicate that regardless of the presence of air holes or dielectric rods, the light wave propagates with a similar degree of bending in both cases. If the curvature is defined as $\Delta\theta = \phi - \theta_m$, where ϕ is the incident angle from x axis and θ_m is the angle at $x/a^{(0)} = m$, then $\Delta\theta = 11.3^\circ$ at $m \sim 60$. This shows that the beam-bending effect produced by the DPC is wholly separate and distinct from the more conventional and well-understood effect of curved propagation in GRIN media. Instead of the GRIN effect, the curvature agrees well with the exact solutions of the geodesic equation [22].

III. EXPERIMENTAL VALIDATION

A. Sample preparation

To experimentally verify the beam deflection phenomenon in a DPC, we fabricate an air-hole DPC in an intrinsic silicon slab. The air-hole structure is favored over dielectric rods for structural integrity reasons; for example, a dielectric slab that is perforated with air holes can be self-supporting [25–30], but rod arrays require a support structure. To ensure a homogeneous refractive index, the radii of the air holes must be changed to compensate for the variation in the interval between the air holes, as described in Sec. II. Consequently, the edges of adjacent air holes come closer and finally connect with increasing n. Considering the fabrication precision for such small intervals, we prepared samples with microscale feature sizes, corresponding to the terahertz regime.

Two samples were devised to support the experimental verification: a uniform square-lattice PC and a DPC. Figure 2 shows the design of these sample structures, as well as micrographs at specific positions that are indicated in the design. The square-lattice PC and DPC were arranged with one input (port A) and two output ports (ports B and C), as shown in Figs. 2(a) and 2(b). Both PCs were designed with $a^{(0)} = 200$ μm and $r^{(0)} = 80$ μm ($= 0.4\, a^{(0)}$), and $\beta = 0.001845$ for

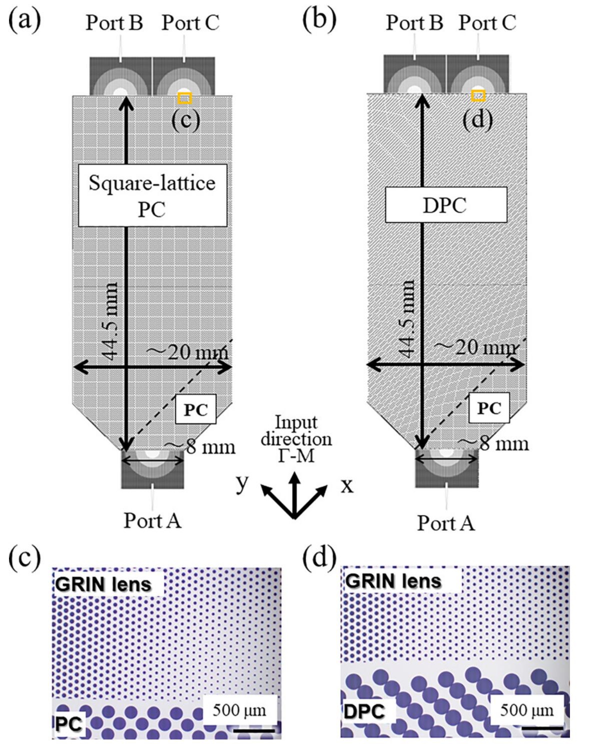

FIG. 2. Design of (a) square-lattice PC and (b) DPC. Both samples have one input port (port A) and two output ports (ports B and C), which use a GRIN lens structure. (c, d) Micrographs of fabricated samples at the locations indicated in (a) and (b), respectively.

the DPC. The β value is selected subject to consideration of two issues. First, β must be maximized to accentuate the steering effect while avoiding physical connection between adjacent air holes, which would compromise the structural integrity of the sample. Figures 2(c) and 2(d) show that the air holes of the DPC are larger than those of the square-lattice PC, but the structure remains self-supporting despite the physical connection between the holes. Second, plane wave excitation is required to avoid strong diffraction within the PC slab, and all ports are coupled to GRIN lenses that interface between a diffraction-resistant in-slab collimated beam and a channel waveguide [31,32]. The physical structure and performance of the lenses have been discussed in detail [32]. The lens that is coupled to port A launches a plane wave into the DPC medium, and ports B and C subsequently collect the power following transit through the sample and convey it to a receiver. The beam width of the plane wave generated from port A is ~8 mm when the input EM wave frequency is 0.3 THz (H mode, normalized frequency is 0.2 for this structure). After passing through port A, the plane wave propagates through the square-lattice PC for a distance of 4 mm along the straight Γ-M line. Subsequently, the plane wave propagates linearly and is then evenly split between ports B and C of the square-lattice PC. For the DPC, the plane wave bends towards port C, causing a discrepancy in the intensity received by ports B and C. As the total propagation length along the straight Γ-M line is 44.5 mm, the effective propagation length in both cases can be calculated using the formula $x/a^{(0)} = 157$.

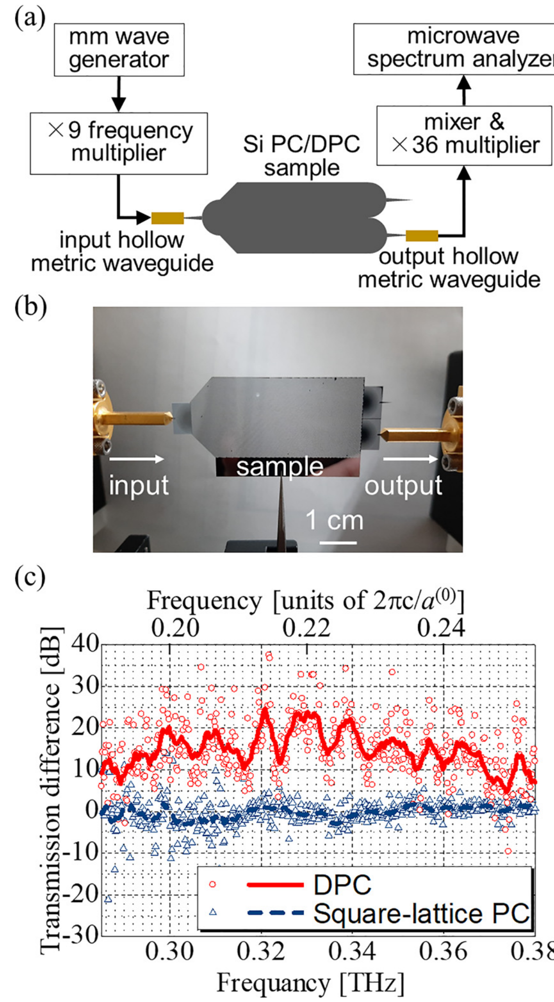

FIG. 3. (a) Schematic diagram of experimental setup. (b) Overview image of experimental setup. (c) Output signal ratio of ports C-B. Dots represent raw data and lines represent rolling average of 15 adjacent raw data. The variation in results is due to Fabry-Perot reflections at the input and output ports [31].

B. Experimental setup and results

Figure 3(a) shows the experimental setup employed to probe the transmission between port pairs A-B and A-C of both the square-lattice PC and the DPC sample. An all-electronic measurement system was employed for this purpose. Terahertz waves are generated by up-conversion of a millimeter-wave signal of 32–42 GHz by a × 9 frequency multiplier and are subsequently conveyed to a hollow rectangular metallic waveguide with inner conductor dimensions 711 μm × 356 μm. A linear tapered spike is situated at the termination of the dielectric channel waveguide that interfaces with the integrated lens at port A. This spike is inserted directly into the hollow waveguide to provide broadband index matching and facilitate efficient flow of power into the silicon sample. Alignment between the silicon sample and the hollow waveguide was performed manually using precise micrometer stages, and the sample was held with ordinary tweezers during probing. A detector is interfaced to the sample via a second hollow metallic waveguide, which is connected to either port B or C. This down-converts the received terahertz power with a mixer and ×36 multiplier, thereby yielding signals that could be displayed by a microwave spectrum analyzer. For both the square-lattice PC and DPC samples, ports B and C are probed in this manner. An overview of the experiment is shown in Fig. 3(b), and the experimental results are shown in Fig. 3(c). For the square-lattice PC, a near-identical intensity is detected across the 0.285–0.380 THz ($\omega a^{(0)}/2\pi c = 0.19 - 0.255$) measurement range. The DPC, on the other hand, shows strong skew toward port C for all frequencies lower than 0.375 THz ($\omega a^{(0)}/2\pi c < 0.25$). The DPC exhibited a ratio of approximately 20 dB in the received intensity between ports B and C in the region of 0.300–0.330 THz ($\omega a^{(0)}/2\pi c = 0.20 - 0.22$).

IV. DISCUSSION OF SIMULATIONS

To evaluate the experimental results, a corresponding numerical simulation with the sample structure was performed using a two-dimensional finite-difference time-domain (FDTD) method, as shown in Fig. 4. To ensure appropriate computational resources, we used a lattice constant of $a^{(0)} = 180$ nm, lattice point radius of $r^{(0)} = 72$ nm ($= 0.4\, a^{(0)}$), $\beta = 0.003$, and an effective propagation length of $x/a^{(0)} = 97$. The β value was determined using the scaling law of DPC (see Appendix A) to miniaturize the entire experimental structure to ∼9%. An EM wave was excited on the Si waveguide by a magnetic dipole, and the input wave was monitored in front of the GRIN lens at port A. The output waves were monitored after passing through the GRIN lenses at ports B and C. Figures 4(b) and 4(c) show the EM wave just after port A and before ports B and C. For the PC, the wave propagates straight and is divided equally between ports B and C. However, for the DPC, the wave is primarily yielded to port C and is skewed due to reflection from the DPC and air interface. The output difference between ports B and C for the PC and DPC is shown in Fig. 4(d). Similar to the experimental results, the DPC exhibited a ratio of approximately 20 dB in received intensity between ports B and C in the region of $\omega a^{(0)}/2\pi c = 0.20 - 0.22$, while the PC had almost 0 dB. It is also important to consider the effects of fabrication errors. Three-dimensional (3D) optical surface profile measurements showed that the etched holes of the experimental sample had a 3° taper along the depth, which changes the H mode to E mode [33]. This change cannot be detected by the detector and does not affect the beam trajectory in the DPC after propagation. Corresponding 3D FDTD simulations with the same propagation length showed an average loss of 4 dB due to the tapered structure. Accounting for this loss, the experimental results validated that the EM wave was curved within the DPC, as designed. Notably, the decrease in the ratio for frequencies higher than 0.375 THz ($\omega a^{(0)}/2\pi c > 0.25$) is caused by the proximity to the band edge, where the low group velocity results in prominent waveguiding loss [27,34] at similar frequencies.

V. CONCLUSION

In this study we numerically and experimentally demonstrated beam deflection by pseudogravity caused by lattice distortion in PCs. Pseudogravity caused by lattice distortion reveals alternative approaches to achieve on-chip trajectory control of light propagation in PCs. The in-plane trajectory curvature has the potential to be applied to the spatial phase control of a beam by combining it with vertical diffraction. Furthermore, it provides a pathway to realize devices that exploit additional gravitational effects such as gravitational lenses and gravitational waves. PC physics have been developed based on the relationship between electron and photonic systems [35–38]. Our results may pave the way for graviton physics.

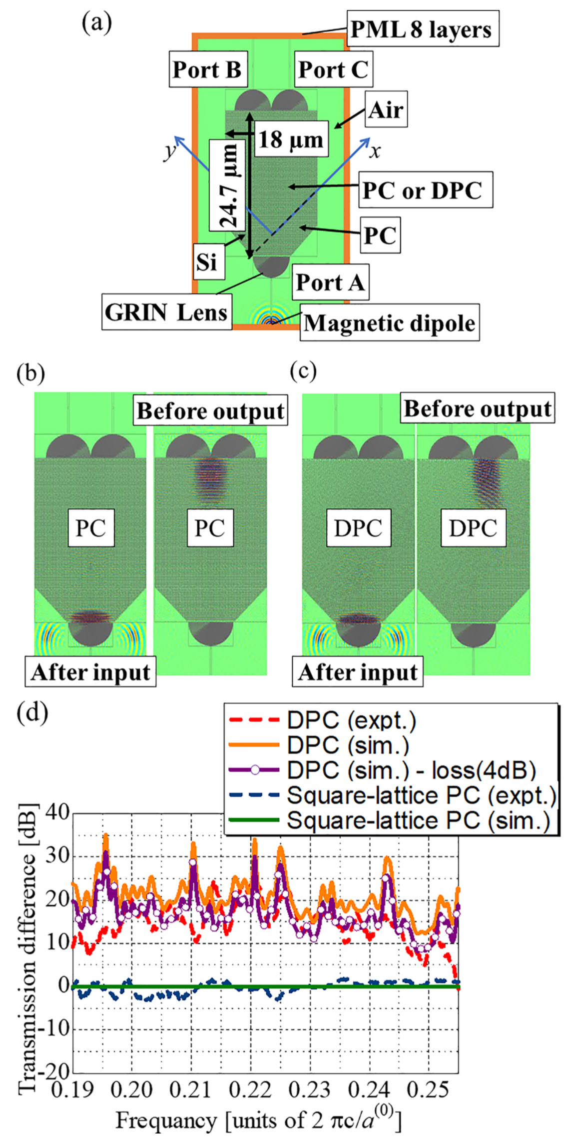

FIG. 4. (a) Simulation model diagram showing the 9% miniaturized version of the experimental structure, where eight perfectly matched layer (PML) absorbing boundaries are employed. The input-output monitor is located on the Si waveguide before port A's GRIN lens or after ports B's and C's GRIN lenses. (b), (c) Light propagation after input and before output for the PC and DPC, respectively. (d) Output signal ratio of ports C-B, where the solid lines represent simulation results and the dashed lines represent experimental results [as shown in Fig. 3(c)]. The upper lines show the results in the case of DPC, and the lower lines show that in the case of PC. The solid purple line with circle accounts for the 4 dB loss due to the tapered air-hole structure.

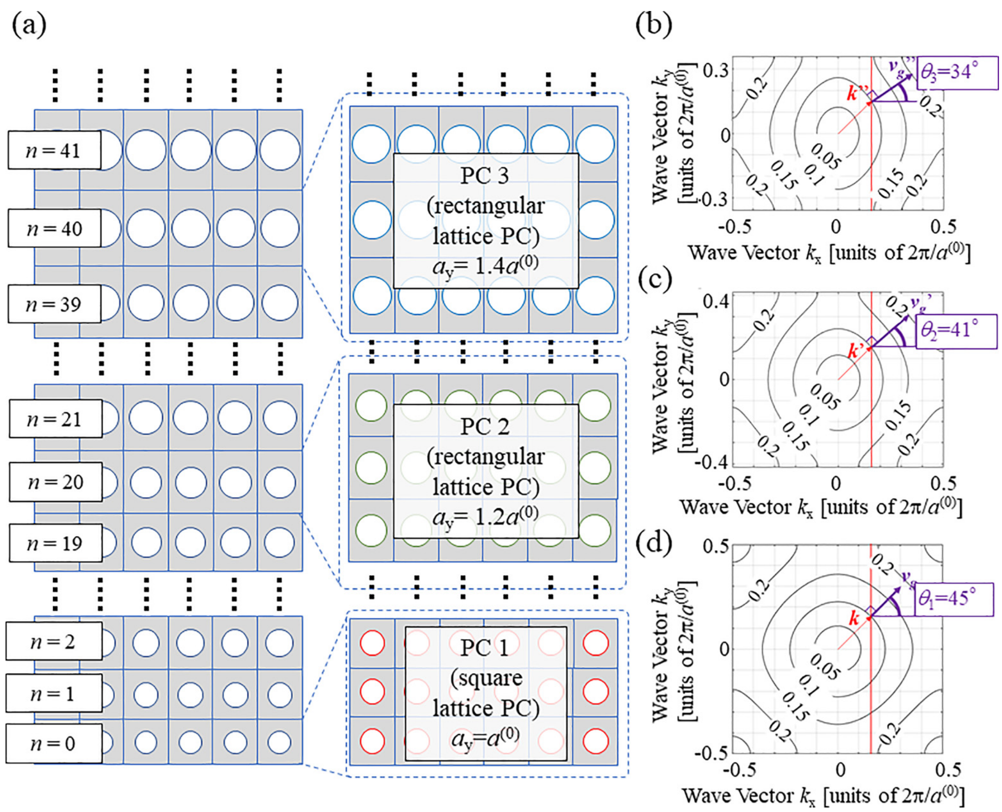

FIG. 5. (a) Schematic of the DPC approximated as a series of PCs: PC1 represents a square-lattice PC, PC2 represents a rectangular lattice PC with $a_y = 1.2a^{(0)}$ (corresponding DPC at $n = 20$), and PC3 represents a rectangular lattice PC with $a_y = 1.4a^{(0)}$ (corresponding DPC at $n = 40$). (b)–(d) Calculation results of EFC in H mode for each PC3–1, respectively. k, k', and k'' represent the wave number vector of light waves propagating in each PC, and v_g, v'_g, and v''_g represent the group velocity vector.

ACKNOWLEDGMENTS

This work was partly supported by JST, PRESTO Grant No. JP20345471, Japan, JST, CREST Grant No. JPMJCR21C4, Japan and JSPS KAKENHI Grants No. JP20H00249, JP22H01991.

APPENDIX A

In this appendix we explain the scaling law of DPC. First, the light trajectory is determined by the exact solution of geodesic equation, which is given as follows (for detailed derivation, see Ref. [22]):

$$y/a^{(0)} = \frac{1}{2\gamma\beta} \ln|2\gamma\beta \tan\phi(x/a^{(0)}) + 1|, \qquad \text{(A1)}$$

where γ represents the weight factor that contains information about undistorted PCs, such as the filling factor, dielectric contrast between the lattice point and background, and inclusion of the second-order perturbative corrections of the eigenvalues for PCs. By substituting $\xi = \beta x/a^{(0)}$ and $\eta = \beta y/a^{(0)}$, the solution can be rewritten as

$$\eta = \frac{1}{2\gamma} \ln|(2\gamma \tan\phi)\xi + 1|. \qquad \text{(A2)}$$

This result shows that the same value of ξ gives the same curvature.

APPENDIX B

Here we present an analysis of the beam deflection in the DPC in terms of the group velocity vector and its variation owing to lattice distortion. The group velocity vector is the slope of the dispersion relation of the PC medium and is the normal vector at the intersection of the wave number vector and EFC. Even when the averaged refractive index, which corresponds to the EFC closed loop area in the low-frequency region, is homogeneous, the direction of the group velocity vector can be changed by a change in the shape of the closed loop. This effect demonstrates that an anisotropic dispersion relation has been induced.

First, we approximated the DPC as a series of uniform PCs with different lattice constants: a square-lattice PC (at $n = 0$) and rectangular PCs (at $n = 20, 40$), as illustrated in Fig. 5(a). The EFC in each region under this approximation was calculated using the plane wave equation method, as shown in Figs. 5(b)–5(d). Using these EFCs, we analyzed wave vector k for light propagation in PC1 at a normalized frequency of 0.1 at 45° from the x axis. The interface component k_x of the wave vector is conserved from the phase-matching conditions at the junction plane of the two media. Therefore, the wave vector in PC2 could be represented as k'. Consequently, angle θ of the group velocity vector changed slightly from $\theta_1 = 45^\circ$ in PC1 to $\theta_2 = 41^\circ$ in PC2. From PC2 to PC3, the group velocity vector changed slightly from $\theta_2 = 41^\circ$ to $\theta_3 = 34^\circ$. At the interface between two types of PCs with the same effective refractive index, the light wave is slightly bent owing to the change in shape of the EFC caused by lattice distortion. Therefore, in DPCs, light rays undergo continuous minor changes of the direction of the group velocity vector, resulting in the trajectory of light propagation bending. Consequently, the anisotropic refractive index induced by lattice distortion was equivalent to the metric tensor identified from the geometry of a DPC.

In the main text, we considered only H mode because the change in shape of the EFC in H mode is distinct. For E mode [E_z polarization, where the electric field is oriented perpendicular to the slab (xy) plane], the trajectory bending is quite small due to the change in EFC shape being almost similar. In terms of this, the DPC can be considered to exhibit the characteristics of structural optical birefringence.

[1] A. Einstein, The foundation of the general theory of relativity, Ann. Phys. (Berlin) **49**, 769 (1916).
[2] F. W. Dyson, A. S. Eddington, and C. Davidson, IX. A determination of the deflection of light by the sun's gravitational field from observations made at the total eclipse of May 29, 1919, Philos. Trans. R. Soc. A **220**, 291 (1920).
[3] A. Einstein, Über Gravitationswellen, K. Preuss. Akad. Wiss., **1**, 154 (1918).
[4] J. Weber, *General Relativity and Gravitational Waves* (Dover Publications, New York, 1961).
[5] B. P. Abbott *et al.* (LIGO Scientific Collaboration and Virgo Collaboration), Observation of Gravitational Waves from a Binary Black Hole Merger, Phys. Rev. Lett. **116**, 061102 (2016).
[6] L. Dong and Q. Niu, Geometrodynamics of electrons in a crystal under position and time-dependent deformation, Phys. Rev. B **98**, 115162 (2018).
[7] R. A. Shelby, D. R. Smith, and S. Schultz, Experimental verification of a negative index of refraction, Science **292**, 77 (2001).
[8] J. B. Pendry, D. Schurig, and D. R. Smith, Controlling electromagnetic fields, Science **312**, 1780 (2006).
[9] C. Pfeiffer, N. K. Emani, A. M. Shaltout, A. Boltasseva, V. M. Shalaev, and A. Grbic, Efficient light bending with isotropic metamaterial Huygens' surfaces, Nano Lett. **14**, 2491 (2014).
[10] Y. Li and Q. Zhu, Broadband birefringent metamaterial lens with bi-functional high-gain radiation and deflection properties, Opt. Express **26**, 16265 (2018).
[11] S. Maurya, M. Nyman, M. Kaivola, and A. Shevchenko, Highly birefringent metamaterial structure as a tunable partial polarizer, Opt. Express **27**, 27335 (2019).
[12] U. Leonhardt, Optical conformal mapping, Science **312**, 1777 (2006).
[13] P. Piwnicki, Geometrical approach to light in inhomogeneous media, Int. J. Mod. Phys. A **17**, 1543 (2002).
[14] T. G. Philbin, C. Kuklewicz, S. Robertson, S. Hill, F. König, and U. Leonhardt, Fiber-optical analog of the event horizon, Science **319**, 1367 (2008).
[15] U. Leonhardt and P. Piwnicki, Optics of nonuniformly moving media, Phys. Rev. A **60**, 4301 (1999).
[16] U. Leonhardt and T. G. Philbin, General relativity in electrical engineering, New J. Phys. **8**, 247 (2006).
[17] M. Notomi, Theory of light propagation in strongly modulated photonic crystals: Refractionlike behavior in the vicinity of the photonic band gap, Phys. Rev. B **62**, 10696 (2000).
[18] S. Y. Lin, V. M. Hietala, L. Wang, and E. D. Jones, Highly dispersive photonic band-gap prism, Opt. Lett. **21**, 1771 (1996).
[19] H. Kosaka, T. Kawashima, A. Tomita, M. Notomi, T. Tamamura, T. Sato, and S. Kawakami, Superprism phenomena in photonic crystals, Phys. Rev. B **58**, R10096 (1998).
[20] T. Baba and M. Nakamura, Photonic crystal light deflection devices using the superprism effect, IEEE J. Quantum Electron. **38**, 909 (2002).
[21] J. Upham, B. Gao, L. O'Faolain, Z. Shi, S. A. Schulz, and R. W. Boyd, Realization of a flat-band superprism on-chip from parallelogram lattice photonic crystals, Opt. Lett. **43**, 4981 (2018).
[22] H. Kitagawa, K. Nanjyo, and K. Kitamura, Effective field theory for distorted photonic crystals, Phys. Rev. A **103**, 063506 (2021).
[23] E. Centeno, D. Cassagne, and J.-P. Albert, Mirage and superbending effect in two-dimensional graded photonic crystals, Phys. Rev. B **73**, 235119 (2006).
[24] H. Kurt, E. Colak, O. Cakmak, H. Caglayan, and E. Ozbay, The focusing effect of graded index photonic crystals, Appl. Phys. Lett. **93**, 171108 (2008).
[25] L. Zhang, Q. Zhan, J. Zhang, and Y. Cui, Diffraction inhibition in two-dimensional photonic crystals, Opt. Lett. **36**, 651 (2011).
[26] R. Kakimi, M. Fujita, M. Nagai, M. Ashida, and T. Nagatsuma, Capture of a terahertz wave in a photonic-crystal slab, Nat. Photon. **8**, 657 (2014).
[27] K. Tsuruda, M. Fujita, and T. Nagatsuma, Extremely low-loss terahertz waveguide based on silicon photonic-crystal slab, Opt. Express **23**, 31977 (2015).
[28] D. Headland, X. Yu, M. Fujita, and T. Nagatsuma, Near-field out-of-plane coupling between terahertz photonic crystal waveguides, Optica **6**, 1002 (2019).
[29] D. Headland, W. Withayachumnankul, X. Yu, M. Fujita, and T. Nagatsuma, Unclad microphotonics for terahertz waveguides and systems, J. Lightwave Technol. **38**, 6853 (2020).
[30] Y. Yang, Y. Yamagami, X. Yu, P. Pitchappa, J. Webber, B. Zhang, M. Fujita, T. Nagatsuma, and R. Singh, Terahertz topological photonics for on-chip communication, Nat. Photon. **14**, 446 (2020).
[31] D. Headland, W. Withayachumnankul, M. Fujita, and T. Nagatsuma, Gratingless integrated tunneling multiplexer for terahertz waves, Optica **8**, 621 (2021).
[32] D. Headland, M. Fujita, and T. Nagatsuma, Half-Maxwell fisheye lens with photonic crystal waveguide for the integration of terahertz optics, Opt. Express **28**, 2366 (2020).
[33] Y. Tanaka, T. Asano, Y. Akahane, B-S. Song, and S. Noda, Theoretical investigation of a two-dimensional photonic crystal slab with truncated cone air holes, Appl. Phys. Lett. **82**, 1661 (2003).
[34] E. Kuramochi, M. Notomi, S. Hughes, A. Shinya, T. Watanabe, and L. Ramunno, Disorder-induced scattering loss of line-defect waveguides in photonics crystal slabs, Phys. Rev. B **72**, 161318(R) (2005).

[35] K. Ohtaka, Energy band of photons and low-energy photon diffraction, Phys. Rev. B **19**, 5057 (1979).

[36] E. Yablonovitch, Inhibited Spontaneous Emission in Solid-State Physics and Electronics, Phys. Rev. Lett. **58**, 2059 (1987).

[37] S. John, Strong Localization of Photons in Certain Disordered Dielectric Superlattices, Phys. Rev. Lett. **58**, 2486 (1987).

[38] F. D. M. Haldane and S. Raghu, Possible Realization of Directional Optical Waveguides in Photonic Crystals with Broken Time-Reversal Symmetry, Phys. Rev. Lett. **100**, 013904 (2008).